

Fracture Along Deformation Twin Boundary in Small-Volume Fe₄₀Mn₄₀Co₁₀Cr₁₀ High Entropy Alloy

Ya-Bo Wang, Ping-Jiong Yang, Xun Sun, Hua-Lei Zhang, and Wei-Zhong Han*

High-entropy alloys (HEAs) with extraordinary combination of strength, ductility, and toughness have drawn extensive attention in recent years. One of widely accepted explanations for the marked mechanical performance in bulk HEAs is due to the tendency of deformation twinning. Here, the authors perform in situ tensile test on small-volume non-equiatomic Fe₄₀Mn₄₀Co₁₀Cr₁₀ HEA single crystals, and find that deformation twinning is a typical intrinsic factor for accelerating fracture. Profuse needle-like deformation twins are nucleated under loading, while their thickening is very difficult due to high twin boundary migration energy, thus nanoscale surface crack is easily produced, which triggers catastrophic fracture.

High entropy alloy (HEA) has attracted extensive research attention recently owing to its promising mechanical, radiation, and corrosive properties.^[1–4] It is well known that, different alloys have different entropy, and the more elements, the higher entropy. As a result of mixing multiple components, HEAs have some character properties, for example, high thermal stability,^[5] excellent mechanical properties,^[6] radiation tolerance,^[7] because of the heavy lattice distortion,^[8] and the sluggish diffusion.^[9] Based on these principles, profuse HEAs have been designed intended for various potential applications.^[10–13]

HEAs are found to display excellent damage tolerance with high strength and high ductility.^[14,15] Deformation twinning is a popular deformation model in HEAs owing to the negative or near zero stacking fault energy.^[16] The combination of dislocation slip and twinning in HEAs provides a steady source of strain hardening to inhibit necking, hence ductility is enhanced together with strength.^[14] The mechanical properties of HEAs can be further enhanced at cryogenic temperatures because of nano-twinning is a

prominent mode of deformation.^[17] Several detailed strengthen mechanisms were proposed based on in situ experiments, for example, the easy glide of Shockley partials, interaction between dislocations and stacking-fault parallelepipeds, arresting at planar slip bands of dislocations and twinned nanoscale bridges etc.^[14] A three-dimensional hierarchical twin network was also reported to form in HEAs.^[18] The twin-network not only serves as blockage of dislocations impinging on twin boundaries, but also offers pathways for dislocation glide along, and cross-slip between, which provide a continuous source of strength, ductility,

and toughness.^[18] Recent studies show that the twin boundary (TB) migration energy in HEAs is quite high,^[19] hence deformation twins in HEAs are easily to nucleate but very difficult to thicken. Since the TB serves as a preferential dislocation glide plane in face-centered cubic (FCC) HEA,^[20] if intense dislocation slip along one major TB in HEAs, it would induces slip steps at grain boundary or at surface, thus leads to stress concentration and promote internal/surface crack development. Actually, sliding of TBs in FCC metals is not very common unless the Schmid factor for leading and trailing partials are equal.^[20–24] If such a deformation model is triggered, twinning would has a negative effect on the plasticity of HEAs. However, no related research was performed to clarify this hypothesis in HEAs.

In this study, we performed in situ tensile tests on single crystalline small-volume Fe₄₀Mn₄₀Co₁₀Cr₁₀ HEAs at room temperature. The bulk non-equiatomic Fe₄₀Mn₄₀Co₁₀Cr₁₀ HEA deforms by planar dislocation slip at low strains (<10% true strain) and deformation twinning at high strains (>10% true strain),^[25] thus it is a right model system to further explore the role of deformation twinning in plasticity of small-volume HEAs. We found that the deformation twins can be easily nucleated, while their thickening is difficult due to high TB migration energy, which promote nanoscale surface crack nucleation and catastrophic fracture.

The non-equiatomic Fe₄₀Mn₄₀Co₁₀Cr₁₀ HEA alloy was melted in a vacuum induction furnace from metals with purities above 99.8 wt% and cast into a water-cooled copper mold following furnace-cooling. One piece of sample cutting from the as-cast ingot was cold rolled to a reduction of 70% from an initial thickness of 3.6 mm to a final thickness of 1.08 mm. The sample was then subjected to a homogenization treatment at 800 °C for 1 h and subsequently quenched in water. Thin foils for microstructure characterization were mechanically ground to about 70 μm in thickness, then further thinned by twin-jet electrochemical polishing in an electrolyte of 10% perchloric

Prof. W.-Z. Han, Y.-B. Wang, P.-J. Yang
Center for Advancing Materials Performance From the Nanoscale & Hysitron Applied Research Center in China
State Key Laboratory for Mechanical Behavior of Materials
Xi'an Jiaotong University
Xi'an 710049, P. R. China
E-mail: wzhanxjtu@mail.xjtu.edu.cn

X. Sun, Prof. H.-L. Zhang
Center of Microstructure Science
Frontier Institute of Science and Technology
State Key Laboratory for Mechanical Behavior of Materials
Xi'an Jiaotong University
Xi'an 710049, P. R. China

 The ORCID identification number(s) for the author(s) of this article can be found under <https://doi.org/10.1002/adem.201801266>.

DOI: 10.1002/adem.201801266

acid and 90% alcohol at -30°C . By using focused ion beam (FIB) micromachining, we fabricated a series of small-volume single-crystal $\text{Fe}_{40}\text{Mn}_{40}\text{Co}_{10}\text{Cr}_{10}$ tensile samples for in situ tensile tests. The dimension of tensile sample is $1\ \mu\text{m}$ (gauge) \times $400\ \text{nm}$ (width) \times $150\ \text{nm}$ (thickness). In situ tensile tests were performed by using a Hysitron PicoIndenter (PI95) equipped with a tungsten grip inside an FEG JEOL 2100F Transmission Electron Microscopy (TEM, 200 kV) under displacement control with speed of $10\ \text{nm s}^{-1}$, corresponding to a strain rate of $5 \times 10^{-3}\ \text{s}^{-1}$. Nine samples with different orientations were explored in this study, as listed in **Table 1**.

Ab-initio calculations were performed using the exact muffin-tin orbitals (EMTO) method^[26] with the single-site coherent potential approximation (CPA).^[27] The Perdew-Burke-Ernzerh (PBE)^[28] form of the generalized gradient approximation is used to approximate exchange and correlation energy. The one-electron equations were solved within the scalar-relativistic approximation and soft-core scheme. We include s , p , d , and f orbitals in EMTO basis. To solve the Green's function, 16 complex energy points distributed exponentially on a semicircular contour containing the valence states below the Fermi level. After carefully test, the Brillouin zones were sampled with 800–1000 uniformly distributed k -points. The screened impurity model parameter^[29] of CPA is 0.6 in present work. The paramagnetic (PM) state of $\text{Fe}_{40}\text{Mn}_{40}\text{Co}_{10}\text{Cr}_{10}$ alloy was described by the disordered local magnetic moment (DLM) approach.^[30,31] We calculate the GSFE using a 12-layers supercell with and without one fault.^[32] The general stacking fault energy (GSFE) is calculated as $\gamma_{\text{GSFE}} = (F_{\text{fault}} - F_0)/A$, where F_{fault} and F_0 are the free energies in the faulted and perfect lattice, respectively, and A is the area of the stacking fault. We adopt the experimental lattice constant $3.621\ \text{\AA}$ ^[25] at room temperature to calculate the GSFE of $\text{Fe}_{40}\text{Mn}_{40}\text{Co}_{10}\text{Cr}_{10}$. We also considered the magnetic entropy, according to the free energies, $F = E - TS_{\text{mag}}$, where E is the total energies, and T is the temperature. The magnetic entropy $S_{\text{mag}} = k_B \sum_{i=1} c_i \ln(1 + \mu_i)$ is estimated within the mean-field

approximation, where k_B is the Boltzmann constant, c_i is the concentration, and μ_i is the local magnetic moment of the i th alloying element.

Figure 1 shows the in situ tensile deformation of a single crystalline $\text{Fe}_{40}\text{Mn}_{40}\text{Co}_{10}\text{Cr}_{10}$ with loading axis of $[1\bar{7}\bar{7}]$. After yielding, the stress-strain curve displays several strain bursts before final fracture, as labeled by b1 to b6 in **Figure 1a**. These strain bursts are caused by the nucleation of twins and their propagation, as shown by the consecutive snapshots in **Figure 1b**. The first narrow twin with thickness of $\approx 30\ \text{nm}$ was nucleated from the right edge of the sample, then gradually penetrated the whole sample (**Figure 1b2, b3**). With further increasing of the stress, a second twin initiated from the lower part of first twin, and crossed the sample quickly, leaving behind a small step on the right surface, as labeled by arrows in **Figure 1b4 and b5**. Following the formation of the second narrow twin, catastrophic fracture occurred along the second narrow TB, as marked in **Figure 1b6**. The bright and dark field images of the fractured sample are highlighted in **Figure 1c**. The electron diffraction pattern confirms these band structures are deformation twins. At the point of fracture, several new twins with thickness of $30 \pm 5\ \text{nm}$ are nucleated at the left upper part, while these twins ceased inside the sample. These observations indicate that the nucleation of deformation twinning is very easy in $\text{Fe}_{40}\text{Mn}_{40}\text{Co}_{10}\text{Cr}_{10}$ HEA, while they are difficult to expand, and fracture occurs along the TB.

Figure 2 shows the second example of twinning induced fracture in $\text{Fe}_{40}\text{Mn}_{40}\text{Co}_{10}\text{Cr}_{10}$ HEA. The sample was loaded along $[1\bar{3}\bar{3}]$. Similarly, several strain bursts set in after yielding, then followed sudden fracture, as shown in **Figure 2a**. The fractured sample was captured by TEM observation, and some black bands are formed near the fracture plane, as shown in **Figure 2b**. It is obvious that the deformation twin is also the origin of fracture. The fractured sample was further examined by tuning to different zone axis. As shown in **Figure 2c and d**, several wide stacking faults (under both bright and dark field images) are produced in the lower part of the failed sample, which are corresponding to the tiny slip steps formed on the

Table 1. The list of Schmid factors of the highest slip and twin systems, the critical Resolved Shear Stress (CRSS), fracture model, and loading orientation of the tested small-volume $\text{Fe}_{40}\text{Mn}_{40}\text{Co}_{10}\text{Cr}_{10}$ samples.

Loading orientation	Slip system	Maximum Schmid factor	Twin system	Maximum Schmid factor	CRSS/GPa	Fracture model
$[1\bar{7}\bar{7}]$	$\{\bar{1}\bar{1}\bar{1}\}\{110\}/\{\bar{1}\bar{1}\}\{\bar{1}01\}$	0.4289	$\{\bar{1}\bar{1}\}\{21\bar{1}\}$	0.4950	0.5445	Along twin boundary
$[1\bar{3}\bar{3}]$	$\{\bar{1}\bar{1}\bar{1}\}\{110\}/\{\bar{1}\bar{1}\}\{\bar{1}01\}$	0.4297	$\{\bar{1}\bar{1}\}\{21\bar{1}\}$	0.4960	0.5753	
$[1\bar{1}\bar{2}]$	$\{\bar{1}\bar{1}\bar{1}\}\{101\}/\{\bar{1}\bar{1}\}\{011\}$	0.4082	$\{\bar{1}\bar{1}\bar{1}\}\{211\}/\{\bar{1}\bar{1}\}\{121\}$	0.3928	0.6599	
$[1\bar{1}\bar{1}]$	$\{\bar{1}\bar{1}\bar{1}\}\{011\}/\{\bar{1}\bar{1}\bar{1}\}\{101\}/\{\bar{1}\bar{1}\bar{1}\}\{110\}/\{\bar{1}\bar{1}\bar{1}\}\{101\}/\{\bar{1}\bar{1}\bar{1}\}\{110\}/\{\bar{1}\bar{1}\bar{1}\}\{011\}$	0.2722	$\{\bar{1}\bar{1}\bar{1}\}\{121\}/\{\bar{1}\bar{1}\bar{1}\}\{112\}/\{\bar{1}\bar{1}\bar{1}\}\{211\}$	0.3140	0.5338/0.4490/0.3391	
$[1\bar{7}\bar{5}]$	$\{\bar{1}\bar{1}\bar{1}\}\{110\}$	0.4790	$\{\bar{1}\bar{1}\bar{1}\}\{211\}$	0.4839	0.6418	At slip step
$[5\bar{9}\bar{1}]$	$\{\bar{1}\bar{1}\bar{1}\}\{0\bar{1}\bar{1}\}$	0.4960	$\{\bar{1}\bar{1}\bar{1}\}\{112\}$	0.4582	0.5406	
$[\bar{1}\bar{1}\bar{3}]$	$\{\bar{1}\bar{1}\bar{1}\}\{011\}/\{\bar{1}\bar{1}\}\{\bar{1}01\}$	0.4454	$\{\bar{1}\bar{1}\bar{1}\}\{112\}$	0.4286	0.5194	

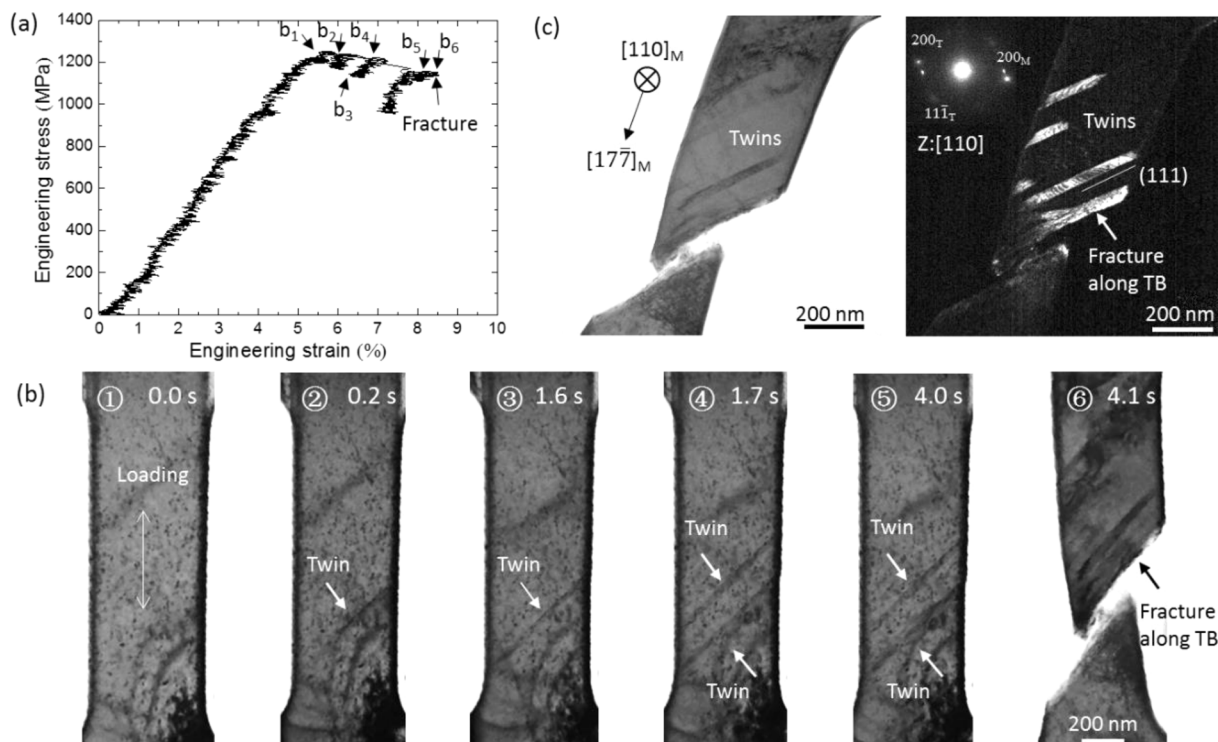


Figure 1. In situ tensile of small-volume $\text{Fe}_{40}\text{Mn}_{40}\text{Co}_{10}\text{Cr}_{10}$ with a loading orientation of $[17\bar{7}]$. a) The engineering strain–stress curve of small-volume $\text{Fe}_{40}\text{Mn}_{40}\text{Co}_{10}\text{Cr}_{10}$ single crystal. b) Snap shots of the in situ tensile video showing the nucleation and growth of twin, and suddenly fracture along twin boundary. c) Post-tensile TEM observation of the fractured sample with multiple deformation twins near the fractured front.

right lateral surface. These results demonstrate that partial dislocation slip is readily in $\text{Fe}_{40}\text{Mn}_{40}\text{Co}_{10}\text{Cr}_{10}$ HEA, whereas deformation twinning is a precursor for brittle fracture.

Figure 3 displays a special example of the plastic deformation of $\text{Fe}_{40}\text{Mn}_{40}\text{Co}_{10}\text{Cr}_{10}$ HEA with loading axis along $[11\bar{2}]$ and view direction near $[\bar{1}11]$. Under this zone axis, possible dislocation slip on $(\bar{1}11)$ can be captured. Figure 3a shows the typical engineering stress–strain curves. The detailed deformation processes can be found the Movie S1. Before tensile loading, there is a full dislocation segment line in the middle of

sample, as shown in Figure 3b1 and Movie S1 (the video is sped up for 2 times). With the gradually increasing of the stress to about 1400 MPa, the dislocation segment starts to bow toward $\langle 110 \rangle$ direction on the $(\bar{1}11)$ plane, as displayed in Figure 3b2 and marked in Figure 3a. The glide of the dislocation segment leaves two screw dislocation lines on the slip plane (Figure 3b3). When stress reaches 1600 MPa, the front part of the dislocation slips out the sample and leaves two dislocation lines with screw character. The screw dislocation lines are immobile under tensile loading in contrast to the easy

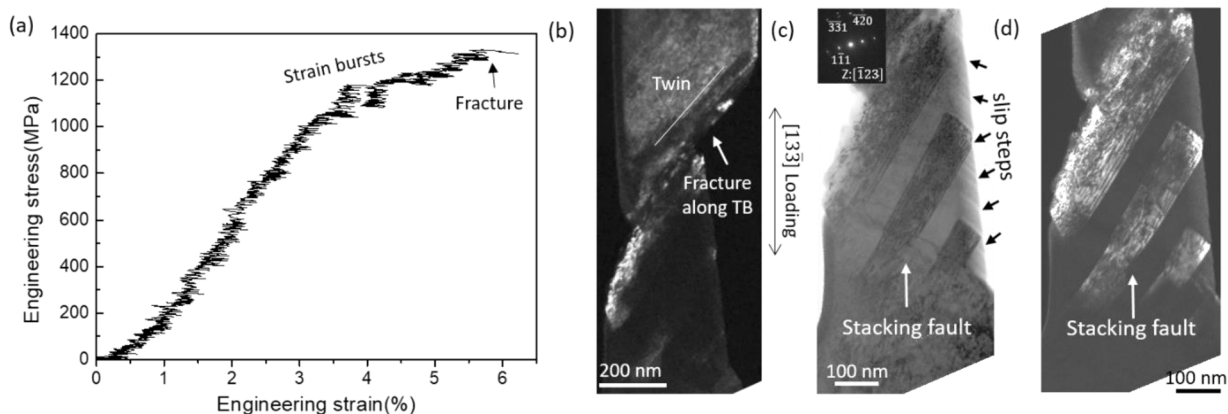


Figure 2. In situ tensile of small-volume $\text{Fe}_{40}\text{Mn}_{40}\text{Co}_{10}\text{Cr}_{10}$, single crystal with a loading axis of $[13\bar{3}]$. a) The engineering strain–stress curve of small-volume $\text{Fe}_{40}\text{Mn}_{40}\text{Co}_{10}\text{Cr}_{10}$, single crystal. b) Dark-field TEM image showing the fracture is initiated from a deformation twin boundary. c) Bright-field TEM image and d) dark-field TEM image of the fractured sample with multiple stacking faults.

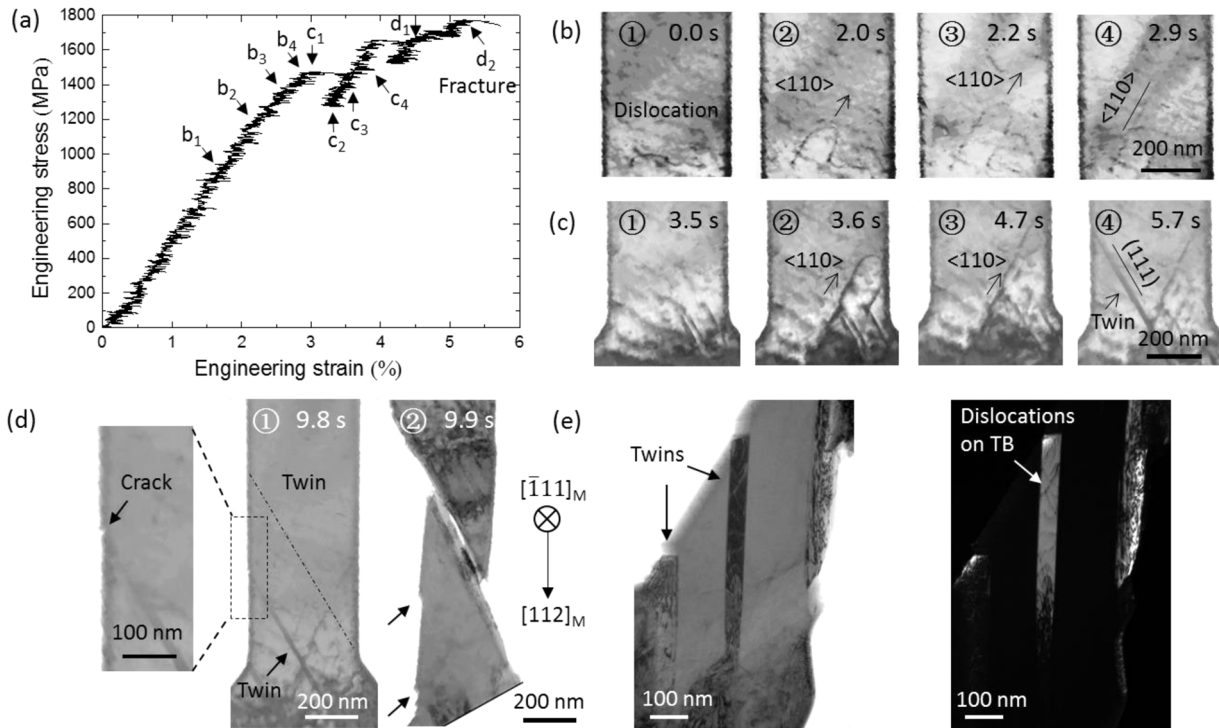


Figure 3. In situ tensile test of small-volume $\text{Fe}_{40}\text{Mn}_{40}\text{Co}_{10}\text{Cr}_{10}$ single crystal with a loading axis of $[112]$. a) The engineering strain-stress curve of small-volume $\text{Fe}_{40}\text{Mn}_{40}\text{Co}_{10}\text{Cr}_{10}$ single crystal. b) The propagation of a pre-existing dislocation segment with increasing of stress, and forming two immobile screw dislocation lines. c) The nucleation of two sets of needle-like deformation twins with further increasing of stress. d) Small crack nucleated once the needle-like deformation twin penetrate the whole sample, and induced sudden fracture along twin boundary. e) Bright-field and dark-field TEM images of the fractured sample showing dislocation lines decorating the twin boundaries. More details can be found in Movie S1.

glide of edge component of dislocations. All these dislocation activities took place in the apparent elastic deformation stage of the sample. Following that, a sudden strain burst sets in on the stress-strain curves, corresponds to the bow out of another dislocation (at the lower right corner of the sample in Figure 3c2), then the dislocation slips out the sample with increasing of the stress, and two screw dislocation lines are formed. Almost at the same time, one sharp needle-like (with thickness of 16 nm) twin quickly nucleates and penetrates the sample along (111) plane, and induces a nano-crack on the left sample surface, as highlighted by left image in Figure 3d. Soon after the formation of first twin, a second needle-like twin penetrates the whole sample and causes fracture, as shown by the right image in Figure 3d. It is obvious that several surface steps are formed on the left surface after sample failure, as marked by the arrows in Figure 3d. These steps are likely the outcome of slip localization along TB during tensile deformation. In order to reveal the formation mechanism of these surface step, we have tuned the sample to make the electron beam near parallel to the TB normal, as shown in Figure 3e. Several dislocation lines are observed on the TB of these deformation twin, as evidenced by both the bright and dark field images. These results indicate that, profuse full dislocations glide along the TB of the deformation twin, and induce a surface step and trigger catastrophic fracture along TB. We have performed more than nine tensile tests on $\text{Fe}_{40}\text{Mn}_{40}\text{Co}_{10}\text{Cr}_{10}$ HEA single crystal, most of them are fractured along TB, while

only a small fraction of samples failed at slip steps, as summarized in Table 1.

Figure 4a plots the loading axis of all the tested samples in the $[001]$ - $[101]$ - $[111]$ inverse pole figure with different symbols to indicate their failure models. Large-scale sliding of coherent TB was reported experimentally when the loading orientation enables the Schmid factors of leading and trailing partials are comparable to each other.^[22] The FCC crystals meet this requirement are marked by the black line and labeled as CTB-sliding in the inverse pole figure (Figure 4a). The samples with orientations located at the right side of the black line deform via detwinning, while the samples with orientations at the left side of black line deform via twinning, nevertheless, both of the cases lead to TB migration.^[22] However, although most of the orientation of small-volume $\text{Fe}_{40}\text{Mn}_{40}\text{Co}_{10}\text{Cr}_{10}$ HEAs single crystals are located at the right side of black line in Figure 4a, most of them showing fracture along TB. The ratio of maximum Schmid factor for twinning and slip are marked in the inverse pole figure as well, as shown by the color coding in Figure 4a. It can be found that the orientations marked by red dots have higher or comparable Schmid factor for twinning than for slipping, thus deformation twinning is favored in these samples, but all of the deformation twins remain at nanoscale and cannot growth under further tensile loading. Under further straining, slip offsets are formed at the intersecting point of TB and free surface, and trigger fractured along TB, which is contradictory with the coherent TB sliding theory of FCC metals.^[22]

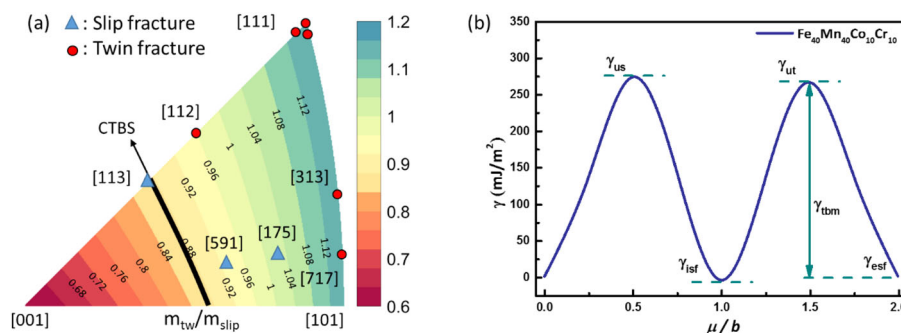


Figure 4. a) The [001]-[101]-[111] inverse pole figure showing the difference in tensile loading orientations of the samples. The samples experienced different fracture model are labelled by blue triangle (slip step fracture) or red point (twin fracture), respectively. The black line in the middle marks the orientations with equal critical resolved shear stresses for slip and twinning according to the Schmid law. b) General stacking fault energy (GSFE) curves for twinning nucleation in $\text{Fe}_{40}\text{Mn}_{40}\text{Co}_{10}\text{Cr}_{10}$. γ_{isf} -intrinsic stacking fault; γ_{us} -unstable stacking fault; γ_{ut} -unstable twinning fault; γ_{esf} -extrinsic stacking fault; γ_{tbm} -twinning boundary migration energy. The shear displacement μ is normalized by the respective Burgers vector b of the partial dislocations.

In order to clarify this puzzle, we have performed further ab initial calculation to determine the migration energy of TB in $\text{Fe}_{40}\text{Mn}_{40}\text{Co}_{10}\text{Cr}_{10}$ HEAs. Similarly to the ordinary FCC metals, the deformation twinning system is $[11\bar{2}]$ (111) .^[25] The GSFE is the energy per unit area required to form N -layers faults, which provides a useful theoretical description of twinning deformation process in FCC alloys. The GSFE for twinning nucleation can be determined by successive shearing 3-layers $\{111\}$ plane over a $1/6[11\bar{2}]$ dislocation. The calculated GSFE curves of the $\text{Fe}_{40}\text{Mn}_{40}\text{Co}_{10}\text{Cr}_{10}$ HEA for twinning nucleation are shown in Figure 4b. We use the following notations: γ_{isf} -intrinsic stacking fault; γ_{us} -unstable stacking fault; γ_{ut} -unstable twinning fault; γ_{esf} -extrinsic stacking fault; γ_{tbm} -twinning boundary migration. The shear displacement μ is normalized by the respective Burgers vector b of the partial dislocations. The obtained GSFE curves of $\text{Fe}_{40}\text{Mn}_{40}\text{Co}_{10}\text{Cr}_{10}$ HEA is comparable with the results of a recent study.^[32]

We can further evaluate the propensity of twinning ('twinability') in the $\text{Fe}_{40}\text{Mn}_{40}\text{Co}_{10}\text{Cr}_{10}$ HEA crystal according to the stacking-fault energy values in Figure 4b. On the basis of Tadmor and Bernstein's work on FCC metals,^[33,34] an empirical expression for twinnability is:

$$\tau_{\text{ta}} = \left[1.136 - 0.151 \gamma_{\text{isf}} / \gamma_{\text{us}} \right] \sqrt{\gamma_{\text{us}} / \gamma_{\text{ut}}} \quad (1)$$

Using this equation, we can calculate the twinnability of current alloy, such as $\tau_{\text{ta}} = 1.154$, which is higher than that of the typical FCC metals with strong tendency for twinning (such as Cu, Ag, and Au),^[35] and comparable to that of CrCoNi HEA^[18] ($\tau_{\text{ta}} = 1.07 \pm 0.02$) and Fe-Cr-Ni TWIP steels^[36] ($\tau_{\text{ta}} = 1.08 - 1.12$), indicating these metals have a high tendency for deformation via twinning under mechanical loading. However, the twinning boundary migration energies $\gamma_{\text{tbm}} = \gamma_{\text{ut}} - \gamma_{\text{esf}}$ is about 266.31 mJ m^{-2} for $\text{Fe}_{40}\text{Mn}_{40}\text{Co}_{10}\text{Cr}_{10}$, which is lower than these of CrCoNi (331 mJ m^{-2}) and CrCoNiFeMn (278 mJ m^{-2}),^[19] but much higher (two times) than that of typical pure metals with medium to low stacking fault energy,^[37] such as $\gamma_{\text{tbm}} = 139.18 \text{ mJ m}^{-2}$ for Cu. The high TB migration energy in HEAs are the fundamental reason for the high energy barrier of thickening of deformation twins, thus they tend to keep at

nanoscale. In addition, the thickness of deformation twins in bulk $\text{Fe}_{40}\text{Mn}_{40}\text{Co}_{10}\text{Cr}_{10}$ is also remained as $18 \pm 15 \text{ nm}$, indicating similar twinning behavior in both bulk and small-volume $\text{Fe}_{40}\text{Mn}_{40}\text{Co}_{10}\text{Cr}_{10}$.^[25] Once dislocation slip localized along TB, large slip steps can be formed very quickly, then stress concentration is built up and induces catastrophic failure along close-packed TB plane, which is the case observed in current in situ tensile tests. In contrast, the slip localization along TB can be suppressed by grain boundaries and neighbor grains in deformation of bulk $\text{Fe}_{40}\text{Mn}_{40}\text{Co}_{10}\text{Cr}_{10}$, thus numerous twinning can be triggered at other locations, as a results, most of the deformation twins are remained at nanoscale after tensile loading.^[25]

In summary, we performed systematic in situ tensile test on small-volume $\text{Fe}_{40}\text{Mn}_{40}\text{Co}_{10}\text{Cr}_{10}$ HEA single crystals, and found that deformation twinning is a typical intrinsic factor for catastrophic fracture. During the tensile loading, profuse needle-like deformation twins are nucleated, while their thickening is very difficult due to the high TB migration energy, thus nanoscale surface crack is easily produced at the intersection of TB and free surface, and trigger catastrophic failure.

Supporting Information

Supporting information is available from Wiley Online Library or from the author.

Acknowledgements

This work was supported by the National Key Research and Development Program of China (2017YFB0702301), the National Natural Science Foundation of China (Grant Nos. 51471128, 51621063), the Innovation Project of Shannxi Province (2017KTPT-12) and the 111 Project of China (Grant No. BP2018008). The authors acknowledge Prof. Feng Jiang for providing the HEA sample.

Conflict of Interest

The authors declare no conflict of interest.

Keywords

deformation twin, fracture, high entropy alloys, in situ, twin boundary

Received: November 28, 2018

Revised: January 13, 2019

Published online: February 20, 2019

-
- [1] J. W. Yeh, S. K. Chen, S. J. Lin, J. Y. Gan, T. S. Chin, T. T. Shun, C. H. Tsau, S. Y. Chang, *Adv. Eng. Mater.* **2004**, *6*, 299.
- [2] B. Cantor, I. T. H. Chang, P. Knight, A. J. B Vincent, *Mater. Sci. Eng. A* **2004**, *375–377*, 213.
- [3] B. Cantor, K. B. Kim, P. J. Warren, *J. Metastable Nanocryst. Mater.* **2002**, *13*, 27.
- [4] L. M. Martyshev, V. D. Seleznev, *Phys. Rep.* **2006**, *426*, 1.
- [5] C. C. Juan, M. H. Tsai, C. W. Tsai, C. M. Lin, W. R. Wang, C. C. Yang, *Intermetallics* **2015**, *62*, 76.
- [6] A. J. Zaddach, C. Niu, C. C. Koch, D. L. Irving, *JOM* **2013**, *65*, 1780.
- [7] T. Nagase, S. Anada, P. D. Rack, J. H. Noh, H. Yasuda, H. Mori, T. Egami, *Intermetallics* **2012**, *26*, 122.
- [8] J. W. Yeh, S. J. Lin, T. S. Chin, J. Y. Gan, S. K. Chen, T. T. Shun, C. H. Tsau, S. Y. Chang, *Metall. Mater. Trans. A* **2004**, *35*, 2533.
- [9] K. Y. Tsai, M. H. Tsai, J. W. Yeh, *Acta Mater.* **2013**, *61*, 4887.
- [10] C. C. Tung, J. W. Yeh, T. T. Shun, S. K. Chen, Y. S. Huang, H. C. Chen, *Mater. Lett.* **2007**, *61*, 1.
- [11] C. P. Lee, C. C. Chang, Y. Y. Chen, J. W. Yeh, H. C. Shih, *Corros. Sci.* **2008**, *50*, 2053.
- [12] F. Otto, Y. Yang, H. Bei, E. P. George, *Acta Mater.* **2013**, *61*, 2628.
- [13] M. H. Tsai, J. W. Yeh, *Mater. Res. Lett.* **2014**, *2*, 107.
- [14] Z. J. Zhang, M. M. Mao, J. Wang, B. Gludovatz, Z. Zhang, S. X. Mao, E. P. George, Q. Yu, R. O. Ritchie, *Nat. Commun.* **2015**, *6*, 10143.
- [15] L. B. Chen, R. Wei, K. Tang, J. Zhang, F. Jiang, L. He, J. Sun, *Mater. Sci. Eng. A* **2018**, *716*, 150.
- [16] J. B. Liu, C. X. Chen, Y. Q. Xu, S. W. Wu, G. Wang, H. T. Wang, Y. T. Fang, L. Meng, *Scr. Mater.* **2017**, *137*, 9.
- [17] B. Gludovatz, A. Hohenwarter, D. Catoor, E. H. Chang, E. P. George, R. O. Ritchie, *Science* **2014**, *345*, 1153.
- [18] Z. J. Zhang, H. W. Sheng, Z. J. Wang, B. Gludovatz, Z. Zhang, E. P. George, Q. Yu, S. X. Mao, R. O. Ritchie, *Nat. Commun.* **2017**, *8*, 14390.
- [19] H. Huang, X. Q. Li, Z. H. Dong, W. Li, S. Huang, D. Q. Meng, X. C. Lai, T. W. Liu, S. F. Zhu, L. Vitos, *Acta Mater.* **2018**, *149*, 388.
- [20] S. Lee, J. Im, Y. Yoo, E. Bitzek, D. Kiener, G. Richter, B. Kim, S. H. Oh, *Nat. Commun.* **2013**, *5*, 3033.
- [21] W. Z. Han, M. S. Ding, R. L. Narayan, Z. W. Shan, *Adv. Eng. Mater.* **2017**, *12*, 1700357.
- [22] Z. J. Wang, Q. J. Li, Y. Li, L. C. Huang, L. Lu, M. Dao, J. Li, E. Ma, S. Suresh, Z. W. Shan, *Nat. Commun.* **2017**, *8*, 1108.
- [23] A. J. Cao, Y. G. Wei, S. X. Mao, *Appl. Phys. Lett.* **2007**, *90*, 151909.
- [24] S. H. Joo, H. Kato, M. J. Jang, J. Moon, C. W. Tsai, J. W. Yeh, H. S. Kim, *Mater. Sci. Eng. A* **2017**, *689*, 122.
- [25] Y. Deng, C. C. Tasan, K. G. Pradeep, H. Springer, A. Kostka, D. Raabe, *Acta Mater.* **2015**, *94*, 124.
- [26] L. Vitos, *Phys. Rev. B* **2001**, *64*, 167.
- [27] L. Vitos, In: *Computational Quantum Mechanicals for Materials Engineers*, Springer-Verlag, London **2007**.
- [28] J. P. Perdew, K. Burke, M. Ernzerhof, *Phys. Rev. Lett.* **1996**, *77*, 3865.
- [29] P. A. Korzhavyi, A. V. Ruban, I. A. Abrikosov, H. L. Skriver, *Phys. Rev. B* **1995**, *51*, 5773.
- [30] B. L. Gyorffy, A. J. Pindor, J. Staunton, G. M. Stocks, H. Winter, *J. Phys. F: Met. Phys.* **1985**, *15*, 1337.
- [31] S. Huang, H. Huang, W. Li, D. Kim, S. Lu, X. Li, E. Holmstrom, S. K. Kwon, L. Vitos, *Nat. Commun.* **2018**, *9*, 2381.
- [32] S. Kibey, J. B. Liu, D. D. Johnson, H. Sehitoglu, *Acta Mater.* **2007**, *55*, 6843.
- [33] E. B. Tadmor, N. Bernstein, *J. Mech. Phys. Solids* **2004**, *52*, 2507.
- [34] N. Bernstein, E. B. Tadmor, *Phys. Rev. B* **2004**, *69*, 094116.
- [35] J. Wang, H. Sehitoglu, *Acta Mater.* **2013**, *61*, 6790.
- [36] W. Li, S. Lu, D. Kim, K. Kokko, L. Vitos, S. K. Kwon, *Appl. Phys. Lett.* **2016**, *108*, 3607.
- [37] Z. H. Jin, P. Gumbsch, E. Ma, K. Albe, K. Lu, H. Hahn, H. Gleiter, *Scr. Mater.* **2006**, *54*, 1163.